J. Geophys. Res., *109*, B08401, doi:10.1029/2004JB002985, 2004

Evidence of fluid-filled upper crust from observations of post-seismic deformation due to the 1992 M_w7.3 Landers earthquake

Yuri Fialko

Institute of Geophysics and Planetary Physics, Scripps Institution of Oceanography, University of California San Diego, La Jolla, California

Abstract. I investigate post-seismic deformation due to the 1992 M_w7.3 Landers, southern California, earthquake using the entire catalog of the ERS Synthetic Aperture Radar (SAR) data, and GPS measurements made between 1992 and 1999. The stacked interferometric SAR data spanning the time period of seven years between the Landers and the Hector Mine earthquakes reveal a transient post-seismic deformation with a characteristic decay time of several years. The horizontal displacements measured with GPS exhibit somewhat smaller decay times of 1-2 years. I use a slip model of the Landers earthquake that fits all available geodetic data [*Fialko*, 2004] to calculate and compare permanent post-seismic displacements due to visco-elastic and poro-elastic relaxation. Visco-elastic models assuming weak mantle or lower crust don't agree with the InSAR data in the limit of complete relaxation, implying either large ($>$ 10 years) relaxation times, or an appreciable yield strength of the lower lithosphere. I demonstrate that a combination of poro-elastic relaxation above the brittle-ductile transition, and localized shear deformation on and below the Landers rupture is able to explain most of the available geodetic data. The InSAR data suggest that pore fluids and interconnected pore space are ubiquitously present throughout the seismogenic layer up to depth of 15 km or greater. The effective hydraulic diffusivity of the upper crust inferred from the kinetics of surface deformation is of the order of 0.1-1 m^2/s, consistent with the laboratory, field, and deep borehole measurements. The post-Landers geodetic data lend support to a "block tectonics" model of the Eastern California Shear Zone.

1. Introduction

Large earthquakes are commonly followed by episodes of decelerating deformation that presumably manifests a time-dependent mechanical response of the host rocks to the co-seismic stress changes. Geodetic and seismic observations in the epicentral areas of shallow earthquakes show that aftershocks account for only a small fraction of the observed deformation, implying that the bulk of the post-seismic relaxation occurs aseismically [*Yagi et al.*, 2001; *Jacobs et al.*, 2002]. The origin and mechanisms of the post-seismic transients are not well understood. Proposed models include enhanced creep on a seismic rupture or its extension below the brittle-ductile transition (the so-called afterslip) [*Savage and Church*, 1974; *Thatcher*, 1983; *Bock et al.*, 1997; *Savage and Svarc*, 1997], poro-elastic rebound of the fluid-saturated crust [*Nikolaevskiy et al.*, 1970; *Booker*, 1974; *Rice and Cleary*, 1976; *Peltzer et al.*, 1998], and visco-elastic relaxation of the ductile lower crust or upper mantle [*Elsasser*, 1969; *Savage and Prescott*, 1981; *Ivins*, 1996; *Pollitz et al.*, 2000]. If various deformation models can be discriminated using geodetic observations, the latter may provide valuable constraints on

the in situ mechanical properties of the host rocks. For example, the spatio-temporal signatures of a surface deformation field may be used to infer the constitutive parameters and depth extent of fault creep in case of the post-seismic afterslip, the presence of fluids and the in situ permeability of the crustal rocks in case of the poro-elastic rebound, and the thickness of the elastic layer, and the rheology of the underlying substrate in case of visco-elastic deformation. Ultimately, such observations may help resolve a long-standing debate about the effective mechanical thickness and strength of the tectonically active continental crust [*England and Molnar*, 1997; *Jackson*, 2002; *Lamb*, 2002]. Unfortunately, interpretation of post-seismic transients is often impeded by the insufficient density and/or accuracy of the available geodetic data, and the fact that different relaxation phenomena may produce quite similar deformation patterns at the Earth's surface [*Savage*, 1990]. The data interpretation is further complicated if more than one mechanism contributes to the observed ground displacements.

One of the best documented examples of the post-seismic relaxation is deformation following the M_w 7.3 Landers earthquake in southern California. The availability of both spatially and temporally dense observations of the post-seismic deformation, including the Interferometric Synthetic Aperture Radar (InSAR) and Global Positioning System (GPS) data, as well as well-constrained models of the causal co-seismic stress changes [e.g., *Hudnut et al.*, 1994; *Wald and Heaton*, 1994; *Fialko*, 2004] make the Landers earthquake a unique test case that may allow robust insights into the nature of the post-seismic relaxation phenomena. The early post-Landers deformation measurements have been interpreted in terms of a number of relaxation mechanisms, including fault afterslip [*Shen et al.*, 1994; *Bock et al.*, 1997; *Savage and Svarc*, 1997], poro-elastic effects [*Peltzer et al.*, 1996, 1998], visco-elastic relaxation in the lower crust [*Deng et al.*, 1998] and upper mantle [*Pollitz et al.*, 2000], compaction of a fluid-saturated fault zone [*Massonnet et al.*, 1996], etc. These models can be now tested against a more complete and extensive space geodetic data set available for an area of $\sim 10^5$ km^2 around the Landers rupture during a time period of ~ 7 years between the Landers and the nearby Hector Mine earthquakes.

The Landers earthquake occurred on June 20, 1992 in the Mojave Desert (Figure 1). The earthquake area has been extensively imaged by the Synthetic Aperture Radar (SAR) satellites of the European Space Agency during 1991-1999 (ERS-1 mission), and since

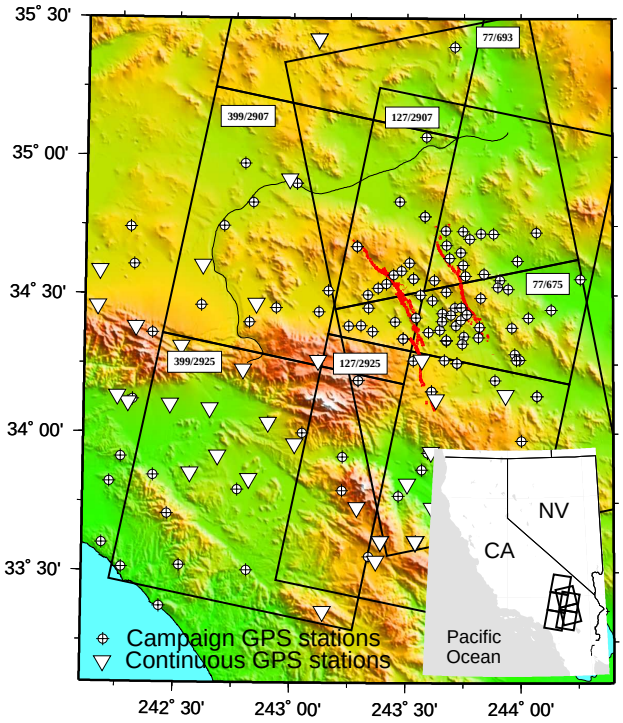

Figure 1. Topography map of the Landers earthquake area. Surface rupture of the Landers earthquake is shown by a thick black wavy line. Solid squares denote ERS radar scenes for the ascending (track 77), and descending (tracks 127 and 399) orbits. Inverted triangles and crossed circles show positions of continuous and campaign-style GPS stations, respectively.

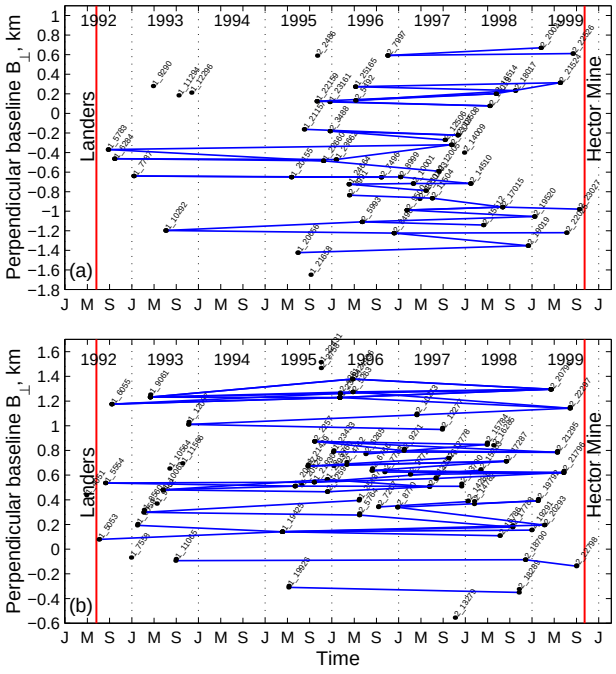

Figure 2. ERS SAR data from (a) track 127 and (b) track 399. Dots denote radar acquisitions (labeled by the platform and orbit numbers). Horizontal axis represents time, and vertical axis represents perpendicular baseline (distance between repeated orbits). Lines connecting dots denote radar interferograms used in this study.

1995 (ERS-2 mission), with more than 200 interferable radar acquisitions available from several satellite tracks (Figures 1 and 2). Because the arid, sparsely vegetated Mojave desert is well suited for radar interferometry, the ERS SAR data provide a unique high-resolution description of the post-seismic surface deformation over a time period of more than 10 years. Another data set of a comparable quality may not become available for the next decade. In addition to the InSAR data, both the co-seismic and post-seismic deformation due to the Landers earthquake have been recorded using continuous and campaign-mode Global Positioning System (GPS) measurements [*Shen et al.*, 1994; *Bock et al.*, 1997; *Savage et al.*, 2003].

In this paper I analyze the time-dependent deformation following the 1992 Landers earthquake using the entire catalog of the ERS SAR data, and the near-field continuous and campaign-mode GPS measurements. The observed ground displacement data are compared to results of theoretical modeling of the post-Landers deformation to establish the presence and relative importance of various relaxation phenomena. One obvious motivation for discriminating the competing theoretical models is a better understanding of the post-earthquake stress changes, and the delayed triggering of seismicity. In particular, identifying a dominant mechanism of the post-seismic deformation might help forecast the evolution of stress and strain fields following large earthquakes, and provide a useful input for the seismic hazard estimates.

2. Satellite interferometry data

The ERS coverage of the Landers earthquake area is shown in Figure 1. Repeated radar acquisitions are available from the descending tracks 127 and 399, and the ascending track 77. InSAR data from different tracks are useful in that they provide different view geometries that reduce (if not resolve) the ambiguity between the horizontal and vertical components of surface deformation intrinsic to the satellite line of site (LOS) measurements [e.g., *Massonnet and Feigl*, 1998; *Rosen et al.*, 2000; *Bürgmann et al.*, 2000; *Fialko et al.*, 2001; *Fialko*, 2004]. The acquired data from the descending tracks are shown in Figure 2. I generated and analyzed all suitable interferometric pairs having perpendicular baselines less than 150 m, and spanning the time period between the Landers and Hector Mine earthquakes (see sub-horizontal lines in Figure 2). Several radar acquisitions not included in this study have either missing data, or unfavorable baselines. The ascending ERS tracks have less frequent acquisitions, and only a few interferograms are available from track 77.

Previous studies based on a few individual post-seismic interferograms [e.g., *Massonnet et al.*, 1994; *Peltzer et al.*, 1998] reported ground displacements having wavelength of the order of kilometers to tens of kilometers, and amplitude of a few centimeters over a few years following the Landers earthquake. The InSAR measurements of a small-amplitude deformation are severely limited by the atmospheric variability. In particular, changes in the water content in the troposphere can generate radar echo delays equivalent to several centimeters (or more) of the LOS displacements of the Earth surface [e.g., *Goldstein*, 1995; *Tarayre and Massonnet*, 1996; *Zebker et al.*, 1997; *Simons et al.*, 2002], i.e., large compared to the inferred post-seismic deformation. In principle, atmospheric effects can be isolated by taking advantage of the redundant InSAR measurements. Averaging of multiple radar interferograms increases the signal-to-noise ratio, and allows

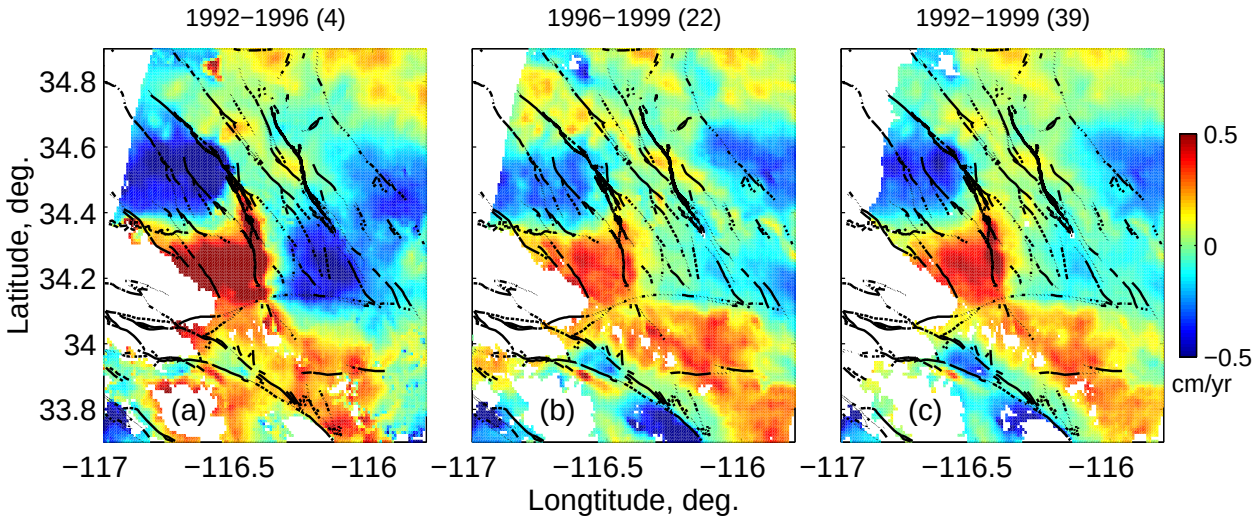

Figure 3. Stacked InSAR data from the ERS track 127. Colors denote the average LOS velocities of the ground, in cm/yr, positive toward the satellite. Black wavy lines denote the Quaternary faults [*Jennings*, 1994]. Titles indicate the time period spanned by the interferometric stack, and numbers in the parentheses correspond to the number of interferograms in the stack.

one to measure LOS displacement rates as low as a few mm/yr [*Peltzer et al.*, 2001; *Fialko and Simons*, 2001]. Figure 3 shows the stacked InSAR data from track 127. Before stacking, each interferogram is spatially averaged over pixel bins 1 km × 1 km. The average LOS velocities are computed by adding the unwrapped interferometric phase from individual pairs, converting the summed phase to the LOS displacements, and dividing the latter by the total cumulative time span of all interferometric pairs in the stack. In order to investigate the time history of the observed deformation, I generate independent stacks of interferograms using data collected over ∼3.5 years following the earthquake (Figure 3a), as well as over the next ∼3.5 years (Figure 3b). A stack of all available data bracketed by the Landers and Hector Mine events (see Figure 2a) is shown in Figure 3c. The InSAR data reveal two pronounced lobes of LOS displacements to the west of the Landers rupture, in agreement with the earlier analysis of *Peltzer et al.* [1998]. The same deformation pattern is also seen in the stacked data from track 399. Figure 4 shows the average LOS velocities along the profile AA′ that traverses the deformation anomaly along the strike of the Eastern California Shear Zone (ECSZ, Figure 3a). Correlated patterns of LOS displacements seen in Figures 3 and 4 demonstrate that the observed signal is due to the post-seismic relaxation and not the atmospheric artifacts. Note that the deformation has persisted after

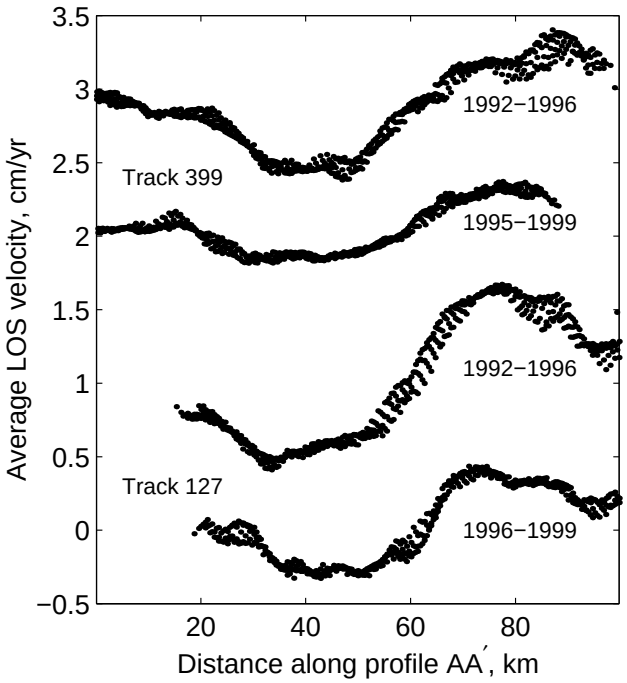

Figure 4. Average LOS velocities inferred from the stacked InSAR data from tracks 127 and 399. Dots denote data from a 3-km wide swath centered on the profile AA′ to the west of the Landers rupture.

1996 (Figure 3b), albeit at a reduced rate, suggesting that the characteristic relaxation time is greater than 0.8 years inferred by *Peltzer et al.* [1998]. It should be pointed out that the signal seen in Figure 3b is apparent only in the interferometric stack, and not in any individual interferogram corresponding to the time period between 1996 and 1999.

Because of a non-linear time-dependent character of the post-Landers relaxation (Figures 3 and 4) it is not straightforward to convert the average LOS velocities derived from stacking of multiple interferograms into the LOS displacements over a given time interval. One way of quantifying a time history of the post-seismic deformation from the InSAR data is to use an a-priori guess for the functional form of time dependence, and solve for some empirical parameters (e.g., a characteristic time constant) that render a good match between the hypothesized time history and the data [*Peltzer et al.*, 1998; *Jacobs et al.*, 2002; *Jonsson et al.*, 2003]. The task is facilitated if the time history of deformation is independent of the spatial coordinate $\mathbf{x}$. The data shown in Figures 3 and 4 indicate that there is no significant spatial dispersion of the deformation anomaly over time. This lends support to the space-time separable representation of the post-earthquake surface displacements D,

$$D(\mathbf{x}, t) = P(\mathbf{x}) \cdot F(t), \tag{1}$$

where t is time elapsed after the earthquake, and $P(\mathbf{x})$ is the permanent post-seismic displacement field (i.e., at $t \to \infty$) [e.g., *Savage et al.*, 2003]. In addition, I shall assume that the time history F is self-similar in that it depends on a non-dimensional ratio t/t_m only, where t_m is some characteristic time scale intrinsic to the physics of the relaxation process. Under these assumptions, it may be possible to evaluate both t_m and $D(\mathbf{x}, t)$ given a sufficient number of interferograms that cover different time intervals of the relaxation period. Let I_j be the observed LOS displacements from the j-th interferogram spanning a time period $\Delta t_j = t_j^{(2)} - t_j^{(1)}$, where $t_j^{(1)}$ and $t_j^{(2)}$ are the respective acquisition times. Correspondingly, let $S_{ik} = \Sigma_{j=1}^{N} I_j$ be a stack of N interferograms collected between times t_i and t_k, where $t_i = \min(t_j^{(1)}, j = 1..N)$, and $t_k = \max(t_j^{(2)}, j = 1..N)$. Under the assumption (1), the ratio of interferometric stacks from different time periods depends on the characteristic decay constant t_m only,

$$\frac{S_{ik}}{S_{mn}} = \frac{\Sigma_{j=1}^{N}\left[F\left(\frac{t_j^{(2)}}{t_m}\right) - F\left(\frac{t_j^{(1)}}{t_m}\right)\right]}{\Sigma_{l=1}^{M}\left[F\left(\frac{t_l^{(2)}}{t_m}\right) - F\left(\frac{t_l^{(1)}}{t_m}\right)\right]}. \tag{2}$$

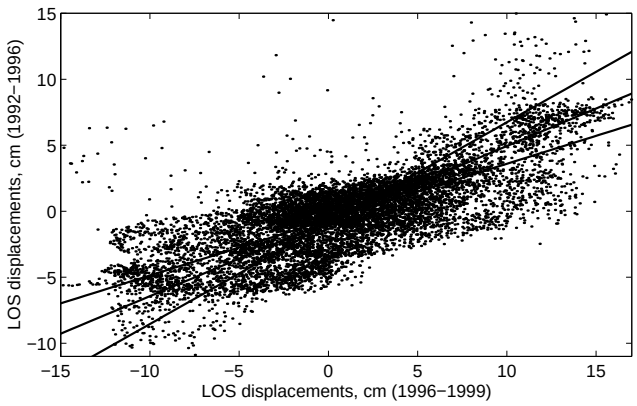

Figure 5. Co-variance of the LOS displacements between interferometric stacks spanning time periods 1992-1996 and 1996-1999, track 127 (see Figures 2a and 3a,b). Dots denote data from pixels within an area 34-35°N, 117-118°W. Lines denote the least squares fit to the data.

Given errors and noise in the data, the ratio S_{ik}/S_{mn} will not be the same for every pixel in the stack. To obtain a robust estimate of the ratio, I perform a linear regression of the stacked LOS displacement data corresponding to the time periods 1992-1996 and 1996-1999. Figure 5 shows the respective regression for data from track 127. A systematic trend seen in Figure 5 is consistent with the assumption (1), and confirms that the deformation process responsible for the early post-seismic relaxation was still active after year 1996. The data scatter in Figure 5 may be due to a number of factors, including the residual atmospheric noise, imprecise orbital corrections, unwrapping errors, any local deformation other than the dominant post-seismic relaxation, as well as deviations of the latter from equation (1). The slope of the reduced major axis of the trend, s_0, is found using a non-biased least squares estimate,

$$s_0 = \sqrt{\frac{\Sigma_{j=1}^{R}\left(S_{ik}^{j} - \bar{S}_{ik}\right)^2}{\Sigma_{l=1}^{T}\left(S_{mn}^{l} - \bar{S}_{mn}\right)^2}}, \tag{3}$$

where S_{ik}^{l} denotes the LOS displacement at the $l-th$ pixel of the stack S_{ik}, R and T are the total number

of data points in the stacks S_{ik} and S_{mn}, respectively, and $\bar{S}_{ik}$ denotes the mean value of the stack, $\bar{S}_{ik} = N^{-1}\Sigma_{l=1}^{N} S_{ik}^{l}$. The slope s_0 given by equation (3) is the best proxy of the ratio S_{ik}/S_{mn} (see middle line in Figure 5). The errors σ_0 in the estimated ratio s_0 are determined as follows,

$$\sigma_0 = \frac{|s_{12} - s_0| + |s_{21} - s_0|}{2}, \qquad (4)$$

where s_{12} and s_{21} represent slopes of the least squares linear fits to the data treating S_{ik} and S_{mn} as independent error-free variables, respectively (Figure 5).

Given the deduced values of the ratio S_{ik}/S_{mn}, acquisition dates of individual interferograms in the stacks S_{ik} and S_{mn}, and some a-priori guess for the functional form of the temporal evolution of deformation $F(t/t_m)$, one can find the respective relaxation time t_m by solving equation (2). It is reasonable to assume that F is a smooth monotonic function that by definition equals zero at $t = 0$ and asymptotically approaches unity at $t \to \infty$ (equation (1)). For example, assuming an exponential decay of the post-seismic displacements, $F = 1 - \exp(-\Delta t/t_m)$, the resulting transcendental equation (2) can be solved numerically to yield $t_m \approx 3 \pm 1$ years. Errors in the solution are estimated using uncertainties in the S_{ik}/S_{mn} ratio (equation (4), Figure 5). The same procedure gives rise to relaxation times $t_m \approx 1 \pm 0.5$ years for the complementary error function $F = \mathtt{erfc}(\sqrt{t_m/\Delta t})$ (which may describe, e.g., early stages of a diffusive process), and $t_m \approx 7 \pm 3$ years for the log-exponential time function $F = (\log(1 + d(\exp(\Delta t/t_m) - 1)) - \Delta t/t_m)/\log d$, where $d = 10$ is an empirical factor, that may be typical of afterslip [see *Perfettini and Avouac*, 2004, for details]. Note that variations in the inferred relaxation times t_m are due to differences in the assumed form of time dependence $F(t)$, and not due to large uncertainties in the estimation procedure. If fact, all of the abovementioned examples give rise to a quite similar temporal evolution of deformation over the observation period between 1992 and 1999. Figure 6 illustrates the time history of LOS displacements for the different assumed forms of $F(t)$ that satisfy data shown in Figure 5. Similar time histories and the respective characteristic relaxation times t_m are obtained from the analysis of InSAR data from the ERS track 399.

Given a quantitative estimate of a time history of deformation $F(t)$, one can use the stacked InSAR data to deduce the amplitude of LOS displacements that occurred during a particular time interval after the earthquake. From equations (1) and (2) one obtains the following expression for the LOS displacements that occurred between times t_k and t_i,

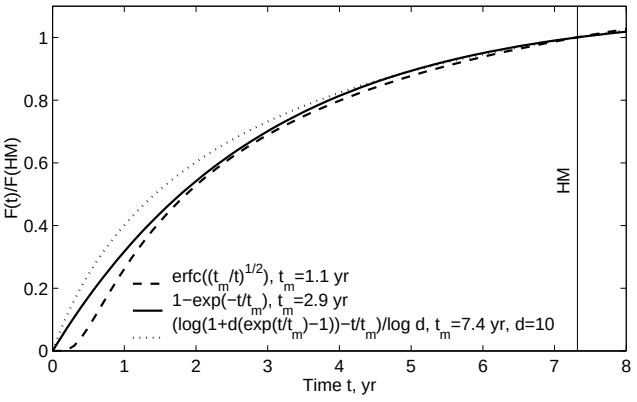

Figure 6. Time dependence of the post-Landers LOS displacements as inferred from the analysis of InSAR data. The theoretical displacement curves are normalized by the displacement accumulated at a particular pixel over a time period between the Landers and the Hector Mine (HM) earthquakes.

$$D(\mathbf{x}, t_i) - D(\mathbf{x}, t_k) = P(\mathbf{x}) \left[F\left(\frac{t_k}{t_m}\right) - F\left(\frac{t_i}{t_m}\right) \right] = S_{ik} \frac{\left(F\left(\frac{t_k}{t_m}\right) - F\left(\frac{t_i}{t_m}\right) \right)}{\Sigma_{j=1}^{N} \left[F\left(\frac{t_j^{(2)}}{t_m}\right) - F\left(\frac{t_j^{(1)}}{t_m}\right) \right]}. \qquad (5)$$

The spatial signature of deformation that occurred over the corresponding time interval is already captured in the interferometric stack S_{ik} (e.g., Figure 3). Thus the right-hand side of equation (5) simply provides a numerical coefficient that converts the amplitude of the stack S_{ik} into the appropriate LOS displacement amplitude. Although the time interval t_k-t_i in equation (5) does not need to coincide with the time span of the stack, numerical experiments indicate that predictions of the signal amplitude beyond the observation interval depend on a particular choice of $F(t)$, and therefore are not robust. For example, the time histories of deformation shown in Figure 6 suggest that by the time of the Hector Mine earthquake, the post-Landers deformation has reached 92%, 65%, or 83% of the permanent fully relaxed state P, assuming the exponential, error function, or logarithmic time dependencies, respectively. For times t_k-t_i within the time span of the stack S_{ik}, inferences of the displacement amplitude D using equation (5) are, on the other hand, nearly independent of a particular choice of $F(t)$. Figure 7

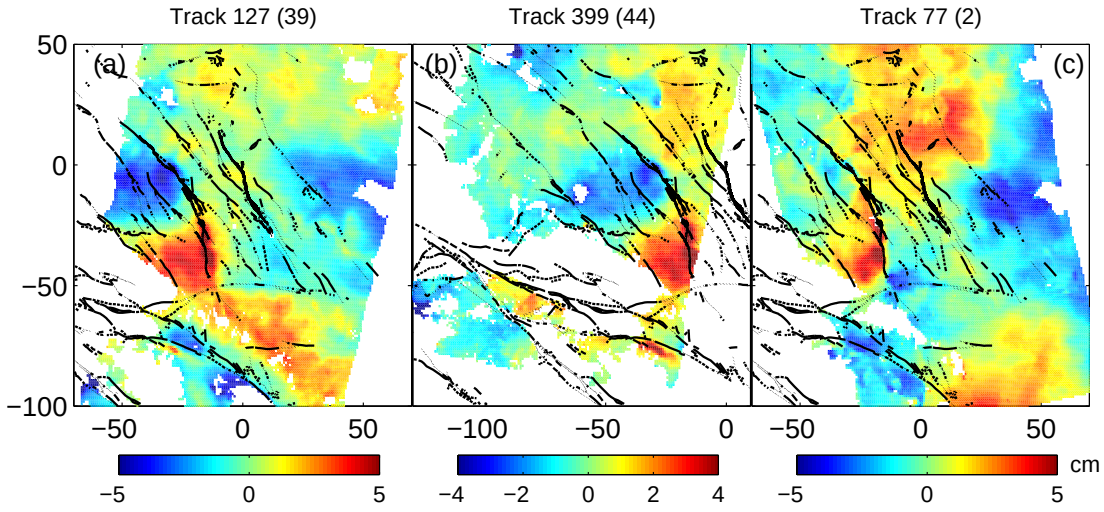

Figure 7. Total LOS displacements accumulated in the interseismic period between the Landers and the Hector Mine earthquakes (1992-1999), in cm. Titles denote the satellite track. Coordinate axes are in km, with origin at the epicenter of the Hector Mine earthquake (116.27°W, 34.595°N). Other notation is the same as in Figure 3.

shows the LOS displacement maps derived from the interferometric stacks using equation (5) for the time period between the Landers and the Hector Mine earthquakes. Calculations using different functional forms of the time history $F(t)$ (Figure 6), as well as various stacking schemes (e.g., accounting for the non-uniform data sampling over time, Figure 2), suggest that the resulting LOS displacements are likely accurate within 10-20% of the inferred amplitude. The data from the ascending orbit (ERS track 77, Figure 7c) represent a sum of only two interferograms spanning the 1992-1999 time interval, and therefore have a much lower signal-to-noise ratio compared to the massively redundant data from the descending orbits (Figures 7a,b).

3. Time-dependent deformation from analysis of GPS data

It is of interest to compare the kinetics of relaxation inferred from the InSAR data to the independent GPS measurements of the post-Landers deformation. The GPS data covering the period of interest (1992-1999) are available from a number of continuous and campaign-surveyed monuments within ∼100 km from the earthquake rupture (Figure 1). Figure 8 shows filtered time series from four continuous PGGA/SCIGN stations closest to the epicentral area (data courtesy of Y. Bock and SOPAC). The co-seismic offsets and the pre-seismic secular trend have been removed from the data to isolate a post-seismic transient. The continu-

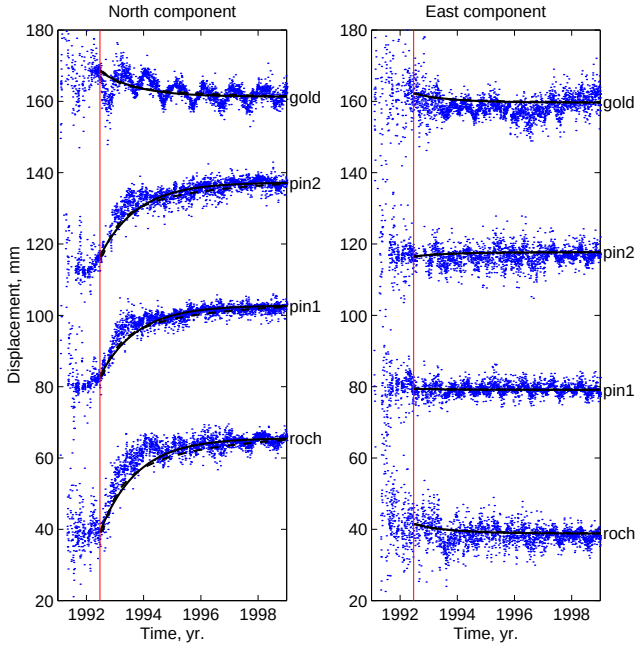

Figure 8. Horizontal components of the post-seismic displacement vectors measured by the continuous PGGA/SCIGN stations. Solid and dashed lines denote the best-fitting exponential (t_m = 1.3 yr) and complimentary error function (t_m = 0.3 yr) approximations, respectively.

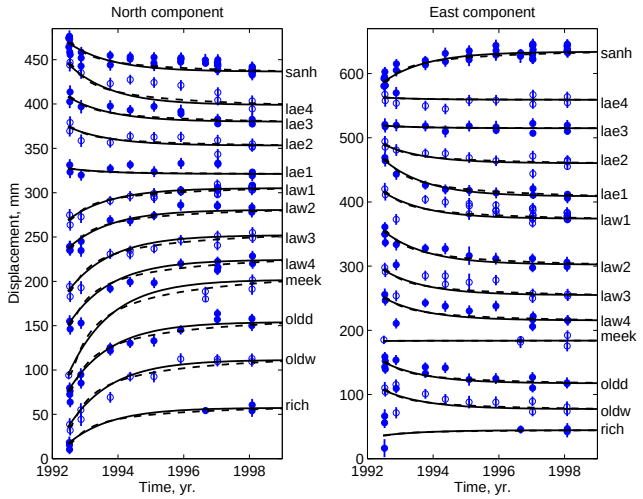

Figure 9. Horizontal components of the post-seismic displacement vectors measured by the USGS campaign surveys in the near field of the Landers rupture [*Savage et al.*, 2003]. Vertical bars denote the formal data errors. Other notation is the same as in Figure 8.

ous GPS data reveal monotonically decaying velocities, sometimes superimposed on periodic seasonal oscillations. Similar velocity transients are also apparent in the campaign GPS data collected by the USGS [*Savage and Svarc*, 1997; *Savage et al.*, 2003]. The USGS campaign GPS time series are shown in Figure 9. There is a significant uncertainty in the magnitude (and even the sign) of the inferred displacement components due to poorly known pre-earthquake velocities of the GPS monuments with respect to the stable North America. Previously published estimates of the interseismic velocity of site Sanh (situated on the eastern side of the southern part of the Landers rupture, see Figure 1) range from 8 ± 3 mm/yr west and 4 ± 4 mm/yr north [*Gordon et al.*, 1993] to 0.6 ± 3.4 mm/yr west and 11.8 ± 2.0 mm/yr north [e.g., *Savage et al.*, 2003]. In the following analysis I use an intermediate velocity of 4 mm/yr west and 6 mm/yr north to account for the relative motion between ECSZ and stable North America.

The time dependence of the GPS data shown in Figures 8 and 9 can be compared to that of the InSAR data, for example, by fitting the GPS time series using the same functional form of the temporal evolution F as in Section 2. The GPS data can be reasonably well approximated by a number of monotonically decaying functions. For the exponential time dependence, the best-fitting decay constant t_m is 1.3 years (solid curves in Figures 8 and 9). For the complementary error function, the best-fitting decay constant is $t_m = 0.3$ years (dashed curves in Figures 8 and 9). While it is possible to fit the campaign GPS time series using larger time constants that agree with the InSAR time series within the estimated uncertainties, such larger time constants would be inconsistent with the continuous GPS data (Figure 8). Therefore it appears that the horizontal displacements measured with GPS decay faster than the LOS displacements measured with InSAR. This difference between the histories of horizontal and vertical deformation is suggestive of more than one mechanism of the post-seismic relaxation.

4. Theoretical predictions of the post-seismic relaxation models

Analysis of the InSAR and GPS data in the previous Sections indicates that deformation following the Landers earthquake was nearly complete by the time of the 1999 Hector Mine earthquake, so that the data shown in Figures 7, 8, and 9 likely capture the bulk of the post-seismic transient. It is instructive to compare the observed deformation to predictions of various post-seismic deformation mechanisms (i.e., afterslip, visco- and poro-elasticity) in the limit of complete relaxation. The fully relaxed solutions are independent of any assumptions about the rock rheology and the time history of deformation, and provide a useful insight into the spatial signatures of the competing models. A qualitative inspection of the observed LOS displacement maps (Figure 7) rules out fault afterslip as the only mechanism of post-seismic deformation. This is because the observed polarity of the LOS displacements (i.e., an apparent uplift in the south-west and north-east quadrants, and subsidence in the north-west and south-east quadrants of the rupture) is opposite to that expected of afterslip above or below the brittle-ductile transition [e.g., *Peltzer et al.*, 1998; *Pollitz et al.*, 2001]. This conclusion is confirmed by inversions of the InSAR data for the distribution of afterslip on the earthquake fault. The inversions failed to produce a reasonable afterslip model assuming that the post-seismic slip is sympathetic with the co-seismic offsets. The sense of the LOS displacements seen in Figures 3 and 7 is consistent with both the visco- and poro-elastic relaxation due to a right-lateral strike-slip earthquake [*Peltzer et al.*, 1998; *Pollitz et al.*, 2000; *Jonsson et al.*, 2003]. To quantify differences between the respective models, I compute the complete visco- and poro-elastic responses due to the Landers earthquake using a slip model that fits all

available space geodetic data [*Fialko*, 2004].

4.1. Permanent deformation due to visco-elastic relaxation

Most models of visco-elastic relaxation using either linear or non-linear rheology of the lower crust or upper mantle assume that (i) all the co-seismically induced change in the deviatoric stress below the ductile transition is eventually relieved by viscous flow, and (ii) the pre-earthquake stress is lithostatic. Hereafter, I will refer to these assumptions as to a "weak substrate" model. As the visco-elastic relaxation gives rise to vanishing co-seismic stress perturbations below a mechanically competent (elastic) upper layer, the fully relaxed response of the upper layer may be obtained using a superposition of two solutions for an elastic half-space. The stress-free boundary condition at the bottom of the elastic layer may be satisfied by applying stresses that are equal in magnitude, but opposite in sign to the co-seismic stress changes at the corresponding depth. The surface displacement field that results from vanishing co-seismic stress changes below the assumed ductile transition are calculated using a boundary element code DIS3D [*Rubin*, 1992; *Fialko and Rubin*, 1999]. First, I calculate the co-seismic displacements at the surface of an elastic half-space using the Landers slip model [*Fialko*, 2004]. The calculation is repeated upon discretizing the assumed ductile transition with boundary elements, and prescribing zero normal and shear stresses on those elements. The difference between the two elastic solutions gives the response of the elastic layer over times greater than the characteristic relaxation time scale. If the elastic-ductile interface also coincides with a density contrast, vertical displacements on that interface will result in some restoring buoyancy forces that will affect both vertical and horizontal displacements at the Earth's surface [e.g., *Pollitz*, 1997]. To account for the effects of gravity in the boundary element simulations I require that the vertical stress σ_{zz} resolved on elements approximating the elastic-ductile interface is coupled to the vertical deflection of the interface z, $\sigma_{zz} = \Delta\rho g z$, where $\Delta\rho$ is the density contrast across the interface, and g is the gravity acceleration. The lateral extent of the boundary element mesh representing the ductile interface is chosen to be twice the flexural wavelength of the upper elastic layer. Numerical simulations indicate that a further expansion of the boundary element mesh does not affect the solution. The accuracy of the boundary element models was tested against the fully time-dependent visco-elastic 3-D finite element calculations for simple sources (e.g., a finite dislocation) [*Hoang et al.*, 2003]. Both techniques gave rise to essentially the same results for the permanent post-seismic deformation.

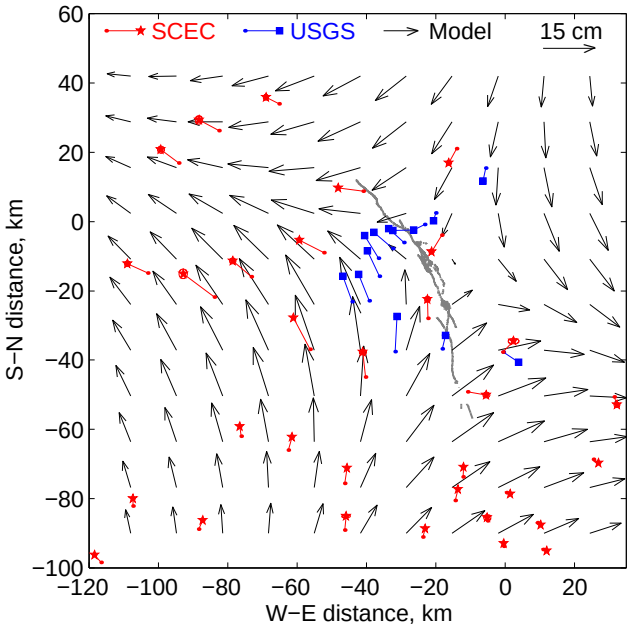

Figure 10. Horizontal displacements observed with GPS over the time period 1992-1999 (starred and squared lines) and predicted by the fully relaxed visco-elastic model (arrows).

Figure 10 illustrates horizontal displacements due to a full visco-elastic response to the Landers earthquake, assuming that the relaxation occurred in the mantle below the depth of 30 km [*Pollitz et al.*, 2000, 2001], and the density contrast across the Moho is $\Delta\rho = 500$ kg/m^3. Also shown in Figure 13 are the GPS measurements of horizontal deformation made within ∼70 km from the Landers available from the USGS [*Savage and Svarc*, 1997; *Savage et al.*, 2003] and SCEC (crustal velocity model CMM2). All GPS vectors represent displacements over a time interval between the Landers and Hector Mine earthquakes corrected for the inter-seismic strain accumulation on the San Andreas fault using a model of *Smith and Sandwell* [2003]. Vectors showing the USGS data represent analytic fits to the GPS time series (see solid and dashed lines in Figure 9). As one can see from Figure 10, predictions of a visco-elastic model agree fairly well with the campaign GPS observations (cf. star and square symbols and arrows in Figure 10), prompting a possibility that the post-Landers transient might be dominated by a viscous relaxation of an abnormally weak mantle below the strong

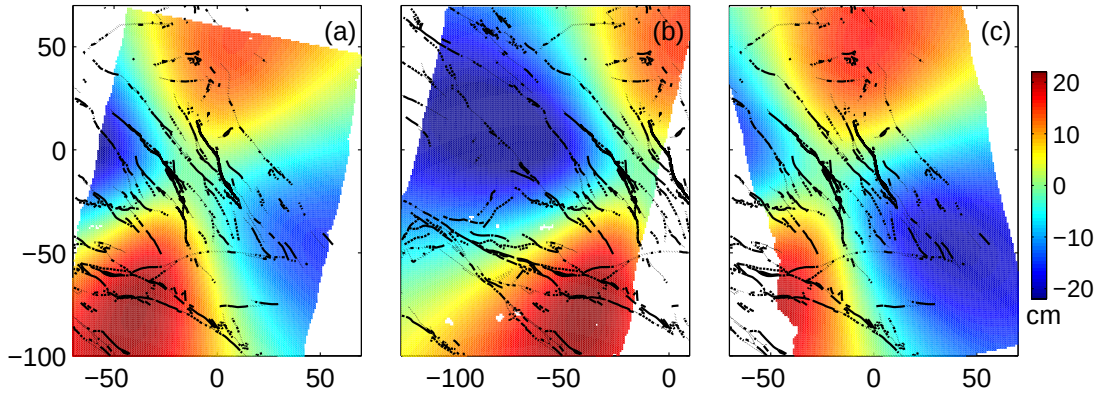

Figure 11. The LOS displacements predicted using boundary element simulations of a complete visco-elastic relaxation after the Landers earthquake, assuming the relaxation depth of 30 km. Figures (a)-(c) correspond to different ERS tracks (see Figure 7).

Mojave crust [e.g., *Pollitz et al.*, 2000]. However, detailed comparisons between the visco-elastic model predictions and both the GPS and the stacked InSAR data caution against such an interpretation. Figure 11 shows the theoretical LOS displacements corresponding to a model of viscous relaxation below 30 km. As one can see from Figure 11, both the wavelength and the amplitude of theoretical displacements significantly exceed the observed ones (in particular, cf. Figure 7b and Figure 11b). Note that the modeled surface displacements depend on the co-seismic slip, but are independent of the shear modulus of the elastic layer.

In order to reconcile the InSAR data with the visco-elastic model predictions one might postulate that the vertical displacements due to crustal flexure reached only a small fraction of the fully relaxed state seven years after the Landers earthquake (so that the bulk of viscous deformation is yet to occur). If so, results shown in Figures 7 and 11 imply a characteristic relaxation time of the order of 10 years or greater, corresponding to the effective mantle viscosity in excess of 10^{19} Pa s. The assumption of an essentially incomplete relaxation does not agree with decay times of a few years deduced from both the InSAR (Figure 6) and GPS (Figures 8 and 9) data. Also, it is inconsistent with an apparent match between the amplitudes of the observed horizontal displacements and those modeled under the assumption of a fully relaxed mantle (Figure 10). The stacked InSAR data reveal high gradients in the LOS displacements across the 1992 surface break (see Figures 3 and 7), in agreement with a previous analysis of *Peltzer et al.* [1998] of an individual interferogram spanning 3.6 years after the earthquake. The observed localized strain on the Landers rupture cannot be caused by any deep relaxation mechanism, and is suggestive of a shallow origin of post-seismic deformation. Although a number of GPS observations can be satisfactorily explained by the viscous relaxation model, the latter significantly overpredicts far-field displacements perpendicular to the main nodal plane of the earthquake (e.g., south of the Landers rupture in Figure 10). Large fault-perpendicular displacements in the far field are a distinctive feature of viscous relaxation [e.g., *Hearn*, 2003]; in particular, such displacements are not typical of afterslip. The same arguments apply to the visco-elastic relaxation in the lower crust. For the fully relaxed solution, decreases in the assumed thickness of the elastic layer give rise to a smaller wavelength, but larger amplitude LOS displacements compared to those shown in Figure 11. However, the transient response of the "jelly sandwich" model of the viscoelastic lower crust gives rise to an inverted polarity of vertical displacements at the surface [*Masterlark and Wang*, 2002], opposite to the observed pattern (Figure 7). Therefore one may conclude that the weak substrate (either upper mantle or lower crust) models do not explain the observed post-Landers deformation, and a consideration of other governing mechanisms is certainly warranted.

4.2. Permanent deformation due to poro-elastic relaxation

In the presence of pore fluids and non-zero permeability in the crust, the co-seismic stress changes will cause fluid withdrawal from areas of an increased hydrostatic stress, and influx into areas of a decreased

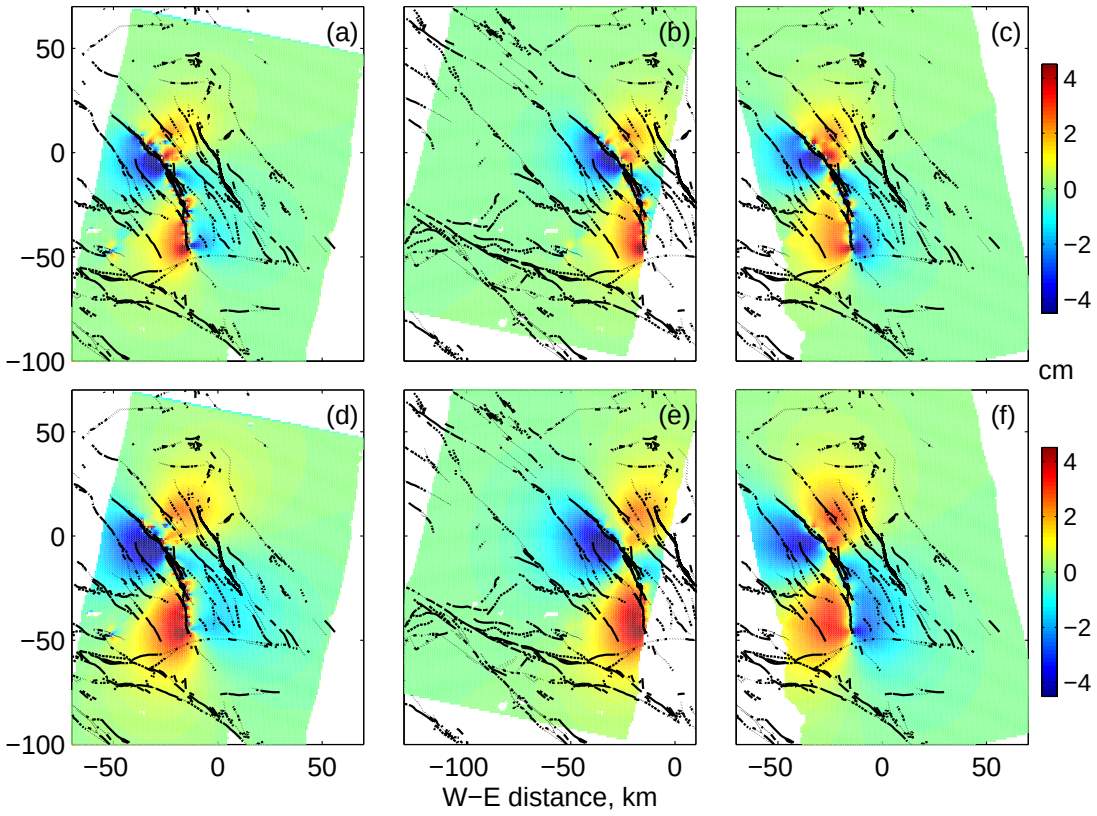

Figure 12. The theoretical LOS displacements due to a complete poro-elastic relaxation after the Landers earthquake, assuming fluid diffusion in the uppermost 2.5 km (figures a-c), and 15 km (figures d-f) of the crust.

Table 1. Effective elastic moduli of the layered half-space model used in the poro-elastic simulations

Layer #	Depth interval, km	Undrained Poisson's ratio ν_u	Drained Poisson's ratio ν_d	Shear modulus, μ^1
1	0-2.5	0.315	0.28/0.215[2]	0.25
2	2.5-5.5	0.176	0.14	0.43
3	5.5-28	0.258	0.20/0.258[3]	0.52
4	> 28	0.271	0.271	1.00

[1]Normalized by the shear modulus of the mantle. [2]Assuming the depth of the fluid-saturated layer of 15 km/2.5 km. [3]Above/below the depth of 15 km.

hydrostatic stress. The resulting diffusion and re-equilibration of pore pressures will effectively decrease the bulk modulus of the crust compared to its "undrained" value immediately after the earthquake [e.g., *Booker*, 1974; *Rice*, 1980]. A fully relaxed poro-elastic signal can be estimated by calculating the surface displacement field due to slip on the Landers rupture using the undrained and drained elastic moduli, subtracting the undrained solution from the drained one, and projecting the residual displacement field onto the respective lines of sight of the ERS satellites. The predicted poro-elastic response depends only on the co-seismic slip model, and the difference between the drained and undrained values of the Poisson's ratio of the crust. I perform several calculations in which the difference between the drained (ν_d) and undrained (ν_u) Poisson's ratios is varied as a function of depth to explore a trade-off between the magnitude of $\nu_u - \nu_d$ and depth of fluid flow. Values of the drained Poisson's ratio are chosen by trial and error to render the best agreement between the model and the InSAR data in the near field (within 10-15 km) of the Landers rupture (Figure 7). Calculations are implemented using a numerical code for a layered elastic half-space [*Wang et al.*, 2003], the undrained elastic structure of the Mojave crust inferred from seismic studies [*Jones and Helmberger*, 1998], and the respective slip model of the Landers earthquake [*Fialko*, 2004]. Figure 12 shows the theoretical LOS displacements due to a poro-elastic relaxation assuming the presence of fluid and interconnected pore space in the uppermost 2.5 km of the crust (Figure 12a-c), and throughout the entire seismogenic layer (above the depth of 15 km, Figure 12d-f). The assumed values of the effective drained and undrained elastic moduli of the crust are listed in Table 1. As one can see from a comparison of Figures 7 and 12, the poro-elastic model assuming relaxation in the entire upper crust reasonably well explains the amplitude, the wavelength, and the spatial details (e.g., high gradients in the LOS displacements across the Landers rupture) of the observed post-seismic deformation. The shallow poro-elastic model requires rather large reductions in the Poisson's ratio (e.g., from 0.315 to 0.215) to explain the observed amplitude of LOS displacements. Even accepting this difference between the undrained and drained Poisson's ratios at face value, the shallow relaxation model conspicuously underpredicts the wavelength of the observed InSAR signal. Therefore one may conclude that if the deformation seen in Figure 7 is primarily caused by the post-seismic diffusion of pore fluids, the latter is likely to involve the entire brittle layer, and perhaps even penetrate into the middle crust. Note that the asymmetry in both the observed and modeled LOS displacements with respect to the fault trace (i.e., larger displacements to the west of the rupture) is due to a contribution of both the horizontal and vertical components of the displacement field to the satellite LOS displacements. On the eastern side of the rupture, projections of horizontal and vertical displacements onto the satellite line of sight have opposite signs, resulting in a destructive interference.

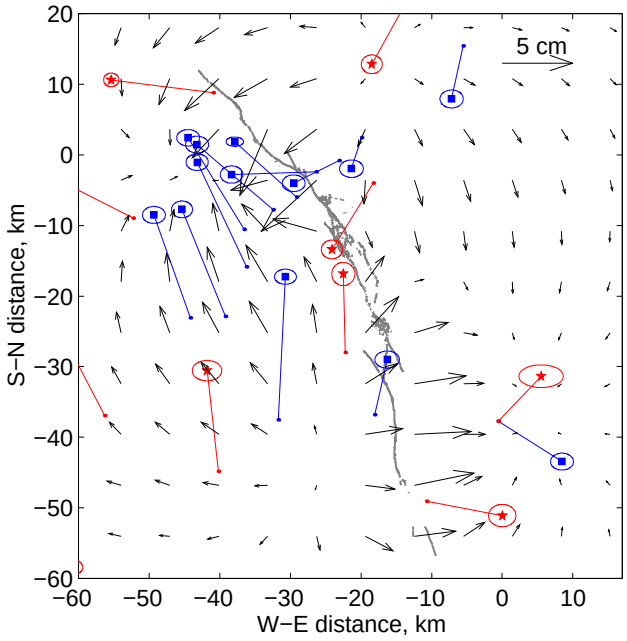

Figure 13. Horizontal displacements observed with GPS over the time period 1992-1999 (starred lines) and predicted by the poro-elastic relaxation model (arrows).

While a poro-elastic model provides a good fit to the InSAR data, it fails to explain the far-field GPS data. Figure 13 shows a horizontal displacement field due to a poro-elastic relaxation in a 15-km thick layer, together with the campaign GPS measurements available from within ∼40 km from the Landers rupture. While the poro-elastic model may help explain some details of the GPS data in the near field of the Landers rupture (in particular, notice the sense of the fault-normal component of the displacement vectors in the northern and southern part of the rupture), the model significantly underpredicts horizontal displacements in the far field. Results shown in Figure 13 are in agreement with earlier estimates of the poro-elastic deformation due to the Landers earthquake [*Peltzer et al.*, 1998; *Masterlark and Wang*, 2002]. If follows that no single mechanism is

able to explain all geodetic measurements of the post-Landers transient.

5. Discussion

Because results presented in Sections 2 and 3 suggest that more than one mechanism is likely to contribute to the observed post-seismic deformation, it is important to establish the relative importance of various relaxation phenomena. Several lines of evidence point out that the weak substrate model explains only a minor (if any) part of the observed deformation. Calculations presented in Figure 11 indicate that if the observed deformation (Figure 7) was due to a viscous flow in the upper mantle or lower crust, the vertical deformation must be less than 20% complete 7 years after the Landers earthquake. This does not agree with characteristic relaxation times of several years deduced from the time series analysis of the InSAR and GPS data (Figures 6, 8, and 9). In the likely case of fluid presence in the upper crust, and the associated poro-elastic response due to the Landers earthquake (Figure 12), the amount of viscous deformation allowed by the InSAR data is smaller still. The limited spatial extent of the post-seismic LOS displacements imaged by InSAR, as well as high gradients in surface displacements across the earthquake rupture (Figure 7) are inconsistent with stress relaxation below the brittle-ductile transition. Although a number of GPS observations can be satisfactorily explained by the viscous relaxation model, the predicted far-field horizontal displacements perpendicular to the main nodal plane of the Landers earthquake are not observed (Figure 10). Finally, the data (e.g., see Figure 3) show no spatio-temporal dispersion of surface strain expected of a stress diffusion in a visco-elastic substrate [*Pollitz*, 1997].

It should be mentioned that some of the spatial signatures of the observed deformation field might be reconciled with a viscous-like response of the lower lithosphere by considering constitutive laws that are more realistic than the visco-elastic Maxwell solid. Given a finite yield strength of rocks below the brittle-ductile transition [*Brace and Kohlstedt*, 1980; *Kirby*, 1983; *Kohlstedt et al.*, 1995], it is reasonable to assume that the post-seismic deformation will relax only those changes in the deviatoric stress that raise the total stress level above the creep threshold. It follows that modeling of the viscous post-seismic response may require an a-priory knowledge of the pre-existing stress. For a strike-slip fault environment such as in the ECSZ, it is likely that the pre-earthquake stress below the brittle-ductile transition is not lithostatic, and the orientation of the maximum shear stress coincides with an overall strike of major faults. The magnitude of shear stress resolved on the downdip extent of the fault zone may be close to the yield strength of the ductile substrate, ensuring a steady state motion in the inter-seismic period. In this case, the co-seismic increases in shear stress along the fault zone may exceed the strength envelope, and be fully relaxed (e.g., by viscous flow). Components of the co-seismic stress change that don't result in excursions of the total deviatoric stress beyond the strength envelope may not be relaxed, and if so will not contribute to the post-seismic transient deformation observed at the surface. Note that the weak substrate (visco-elastic) model predicts a horizontal displacement field resembling pure shear, with comparable magnitudes of the fault-parallel and fault-perpendicular displacements within one rupture length from the earthquake (Figure 10). A more realistic finite strength (e.g., visco-elasto-plastic) rheology of the substrate may give rise to horizontal displacements that are closer to simple shear within the same distance from the earthquake fault. The finite yield strength of the ductile substrate may also prevent relaxation of changes in normal stress at the base of the elastic layer, reducing the amplitude of the post-seismic crustal flexure. Thus a consideration of a long-term strength of the lower lithosphere might explain the absence of large vertical and fault-perpendicular horizontal displacements in the InSAR and GPS data, respectively (Section 4.1). However, the short time scales of the observed deformation transients ranging from months [*Shen et al.*, 1994] to years [Sections 2 and 3; *Savage et al.*, 2003] require an abnormally hot fluid-rich mantle immediately below the Moho [*Pollitz et al.*, 2000, 2001]. As the yield strength of silicate rocks is strongly dependent on temperature and volatile content [*Mainprice and Paterson*, 1984; *Tullis and Yund*, 1987; *Kohlstedt et al.*, 1995], rapid post-seismic deformation appears to be more consistent with the weak substrate model. These arguments suggest that a large-scale viscous deformation did not dominate the post-Landers deformation during the period of observations (1992-1999).

5.1. Preferred post-seismic model

Peltzer et al. [1998] noted that diffusion of pore fluids and fault afterslip give rise to an opposite polarity of vertical displacements at the Earth's surface, and suggested that a combination of the poro-elastic and afterslip mechanisms may explain the pattern of the LOS displacements accumulated between 1992 and

1996. They superimposed a poro-elastic response due to the Landers earthquake (calculated using a co-seismic slip model of *Wald and Heaton* [1994] and assuming a homogeneous elastic half-space) and the afterslip model of *Savage and Svarc* [1997] to find a qualitative match with the observed LOS displacements in the northern part of the fault. The combined model, however, was not directly compared to the GPS data, and rendered a poor fit to the InSAR data around the southern part of the 1992 rupture. Here I test whether both the InSAR and GPS data can be explained by a combination of poro-elastic relaxation and fault afterslip in a self-consistent fashion. I subtract predictions of the best-fitting poro-elastic model (Figures 12d-f and 13) from the InSAR and GPS data, and invert the residuals for the right-lateral slip on the Landers rupture and its downdip extension. Note that the shallow afterslip is subject to some trade-off with the amount of poro-elastic relaxation; the assumption that most of the observed InSAR signal is due to a porous flow effectively puts a lower bound on the amount of both the afterslip and poro-elastic relaxation. Because it is unlikely that the geometric complexity of the Landers rupture persists throughout the lower crust, I assume that the deep afterslip occurs on a plane having an average strike of the ECSZ, and extending vertically from the bottom of the seismogenic layer (15 km) to the Moho (30 km).

Figure 14 shows the horizontal displacement field due the to the best-fitting afterslip model, and the GPS data corrected for the assumed poro-elastic contribution. Calculations are performed using a layered elastic half-space model with drained values of the Poisson ratio (Table 1). The preferred afterslip model is shown in Figure 15, and the residual InSAR data (i.e., LOS displacements not explained by a combination of poro-elasticity and afterslip) are shown in Figure 16. As one can see from Figures 14 and 16, a combined model reasonably well explains most of the available data. The model correctly reproduces the observed pattern of horizontal displacements (in particular, along the main nodal plane of the Landers earthquake, cf. Figures 10 and 14). The model underpredicts the amplitudes of the SCEC GPS vectors further than ~50 km to the west of the rupture. This might indicate either penetration of afterslip below the Moho, or some contribution from a diffuse viscous deformation in the mantle. In the near field, the apparent mistifs between the model and the USGS GPS vectors next to the fault may be due to enhanced poro-elastic effects in the fault step-overs [*Peltzer et al.*, 1996, 1998]. The fit to the near-field GPS data can be improved by allowing several

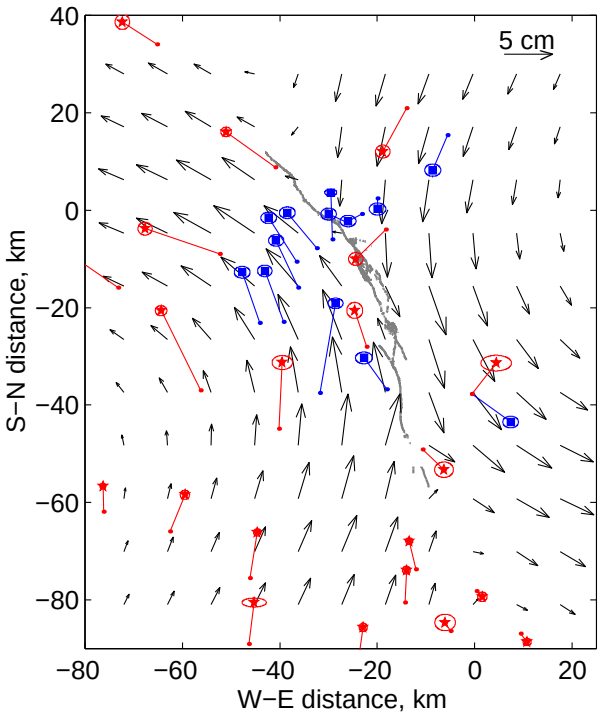

Figure 14. Horizontal displacements due to the fault afterslip model (arrows), and observed with GPS. Notation is the same as in Figure 10.

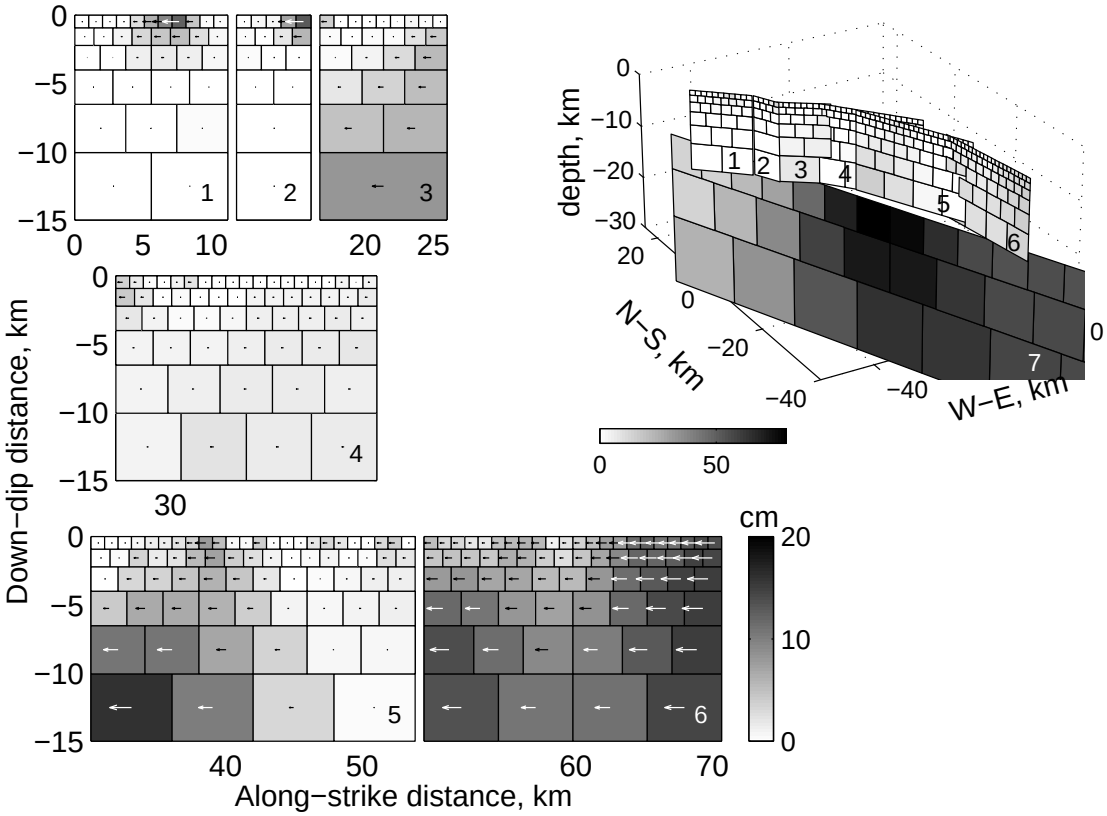

Figure 15. Distribution of right-lateral afterslip on the Landers rupture [segments 1 to 6, see *Fialko*, 2004], and the underlying shear zone (segment 7). Shading and arrows denote the magnitude of slip.

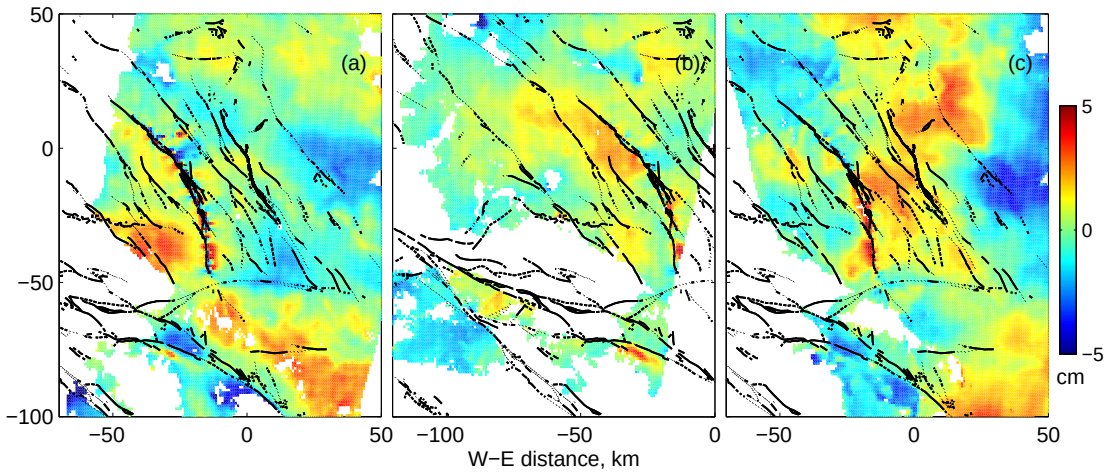

Figure 16. Residual LOS displacements left after subtracting the contributions from the preferred poro-elastic and afterslip models from the stacked InSAR data. Notation is the same as in Figure 7.

centimeters of fault-normal contraction. However, the corresponding reduction in the rms misfit between the model and the data is marginal, and I conclude that the fault contraction is not required by the data. Note that the accuracy of the GPS data is less than the reported formal errors, as evidenced by appreciable differences in the independent GPS solutions available for several sites (Figures 10 and 14); also, error ellipses do not include large uncertainties in the pre-seismic velocities of the GPS monuments (see Section 3). A positive residual of a few cm in the LOS displacements in the south-west quadrant of the Landers rupture in Figure 16a may be due to an underestimated magnitude or depth (or both) of the poro-elastic relaxation, or an uncertainty in the amplitude of the LOS displacements inferred from the stacked InSAR data (e.g., note a centimeter-scale difference in the signal amplitude between different satellite tracks, Figures 7a and 7b). The lateral extent of deep afterslip is poorly constrained by the inversion. *Peltzer et al.* [2001] reported an accelerated accumulation of strain on the Blackwater fault system that links to the northern tip of the Landers rupture, and proposed that the observed strain represents the post-seismic deformation transient. If so, the enhanced creep in the lower crustal shear zone below the Landers rupture may have propagated as far as a few hundred kilometers away from the earthquake fault.

5.2. Physical implications from inverse models

The mechanics of the inferred afterslip may be quite different above and below the brittle-ductile transition. In the lower crust, the accelerated creep below the earthquake fault might represent either frictional sliding under velocity strengthening conditions [*Shimamoto*, 1986; *Tse and Rice*, 1986], or a viscous-like deformation of a localized shear zone that is weaker (and perhaps warmer) than the ambient crust [*Yuen et al.*, 1978; *Fleitout and Froidevaux*, 1980; *Turcotte and Schubert*, 2002, p.369]. As the kinematics of the two processes is nearly identical, they cannot be distinguished based on inversions of geodetic data alone. Inverse models indicate that the amplitude of deep afterslip correlates with the seismic moment release in the brittle layer. In particular, the maximum shear displacement below the brittle-ductile transition (see Figure 15) occurred in an area that experienced maximum co-seismic increases in shear stress [below segment 5, see figure 9 in *Fialko*, 2004]. This distribution, as well as the magnitude of afterslip of the order of one meter, agree with earlier findings of *Savage and Svarc* [1997] who assumed that afterslip occurs on the downdip continuation of the Landers rupture in the depth interval of 10 to 30 km, but did not allowed for any variation of afterslip with depth. The distribution of afterslip seen in Figure 15 is characterized by a maximum slip at the termination of the co-seismic rupture, and a gradual decrease of the slip magnitude with depth. This pattern is consistent with both the velocity strengthening friction and the visco-plastic shear zone mechanisms. Results shown in Figure 15 significantly differ from the afterslip pattern inferred from the GPS measurements of post-seismic deformation due to the 1999 Izmit (Turkey) earthquake [*Reilinger et al.*, 2000]. In particular, the amplitude of afterslip due to the Izmit earthquake was found to increase with depth throughout the lower crust, inversely proportional to the co-seismic stress perturbations.

Above the brittle-ductile transition, the mechanics of afterslip is likely dominated by the rate-and-state friction [*Dieterich*, 1992; *Ruina*, 1983], or the "brittle creep" [*Perfettini and Avouac*, 2004]. The average magnitude of shallow afterslip is about 10-20 centimeters (see subfaults 1 to 6 in Figure 15). Integration of afterslip over the area of the earthquake rupture yields an effective "seismic moment" of $\sim 2 \times 10^{18}$ N·m. A cumulative moment of all aftershocks that occurred within 5 km from the Landers rupture during 1992-1999 is an order of magnitude smaller, indicating that most of the shallow afterslip occurred aseismically. This conclusion is similar to the results of the analysis of geodetic and seismic data from a 1-year period following the nearby Hector Mine earthquake [*Jacobs et al.*, 2002].

An important question is whether the the pore pressure changes associated with poro-elastic relaxation affect the rate and the total amount of afterslip in the upper crust. Theoretical arguments [e.g., *Booker*, 1974; *Rice*, 1980] and numerical simulations (e.g., using dislocation models such as that in Figure 15) indicate that decreases in the effective Poisson's ratio due to the post-seismic re-equilibration of pore pressure increase a sympathetic shear stress on the earthquake fault. The amount of such poro-elastically induced fault re-loading is directly proportional to the co-seismic slip. A comparison of the shallow afterslip (Figure 15) with the co-seismic slip distribution [figure 9 in *Fialko*, 2004] does not show a correlation between the maximum co-seismic and post-seismic slip. Instead, inversion results indicate that the maximum afterslip tends to occur on a periphery of "asperities" characterized by a large co-seismic slip. *Mendoza and Hartzell* [1988] noted a similar spatial relationship between areas of high co-seismic slip and aftershocks. Therefore the co-seismic stress changes appear to exert stronger controls on both the

seismic and aseismic fault slip following a mainshock than the post-seismic pore pressure changes. Different decay times of afterslip and poro-elastic relaxation determined from the near-field GPS and InSAR data (Section 2) also suggest that the spatiotemporal behavior of afterslip may not be tightly coupled to the diffusion of pore fluids.

Given a predominantly volumetric nature of poro-elastic deformation, and a high sensitivity of InSAR to vertical displacements, the kinetics of deformation inferred from the InSAR data may be used to estimate the in situ hydraulic diffusivity of the upper crust, $\kappa_h = L^2/\pi t_m$, where L is the characteristic distance for the fluid diffusion. For L of 5-20 km (corresponding to either a vertical flow from the interior of the brittle layer to the surface, or a horizontal flow between the areas of hydrostatic compression and extension set by the co-seismic stress changes), and a relaxation time t_m of a few years (Figure 6), κ_h is found to be of the order of 0.1-1 m^2/s. This estimate is in a good agreement with laboratory and field measurements of hydraulic diffusivities of fractured crystalline rocks [*Roeloffs*, 1988; *Talwani et al.*, 1999; *Wang*, 2000], including in situ measurements in the super-deep KTB borehole [*Rothert et al.*, 2003]. The estimated relaxation times t_m are also similar to the observed time delays between reservoir impounding or fluid injection in deep wells, and triggered moderate-to-large earthquakes within a few tens of kilometers of either the reservoir or injection well, respectively [e.g., *Healy et al.*, 1968; *Simpson et al.*, 1988]. *Jonsson et al.* [2003] obtained a much shorter decay time of $\sim$ 1 month from the analysis of InSAR and borehole data from a pair of magnitude 6 earthquakes in Iceland. A rapid deformation transient documented by *Jonsson et al.* [2003] may manifest a poro-elastic deformation in the uppermost few kilometers of a highly permeable Icelandic crust. Because the porosity and permeability of crustal rocks are expected to decrease with depth, the longer deformation transient due to the Landers earthquake described in this paper is consistent with fluid percolation involving the entire brittle crust (Section 4).

The stacked InSAR data (Figures 7 and 16) reveal several deformation anomalies that are apparently not related to the post-Landers relaxation, but might be indicative of hydrologic processes in the crust. In particular, a roughly triangular area of negative LOS displacements to the west of the Troy Lake and south of the Mojave river (around coordinate -40,40 km; see, e.g., Figure 16b) seem to be due to a steady state ground subsidence at an average rate of a few mm/yr over seven years of observations. Other areas of ground subsidence are notably associated with Quaternary faults, such as the areas between the northern and southern strand of the San Andreas fault (SAF) near Palm Springs (-25,-70), south of SAF near Salton Sea (0,-90), and to the east of the southern end of the Ludlow fault (30,-10). The inferred subsidence areas exhibit high strains across the faults, perhaps indicating that the latter act as hydrologic discontinuities. This observation is consistent with an assumption that the fault-perpendicular permeability may be much less than the along-fault permeability, implying that active fault zones can develop and maintain elevated pore pressures [e.g., *Rice*, 1992]. Note that the northern boundary of the positive LOS displacement lobe in the south-west quadrant of the Landers rupture coincides with the east-west striking Frontal fault zone (-30,-30, Figures 7a and 16a), which might act as a barrier to the seismically induced pore fluid flow.

Some faults show high gradients in the LOS displacements that may be due to tectonic deformation. A step-like range change across the northern segment of the San Jacinto fault (see an area around -90,-70 km in Figure 16b) may be due to fault creep. The Pinto Mountain fault west of the Landers rupture (10,-50, Figure 16a) appears to be a high strain boundary between the ECSZ, and a topographically elevated block to the south. Unless a region of positive LOS velocities bounded by the SAF and the Pinto Mountain fault represents a residual atmospheric noise, the polarity of the LOS displacements indicate left-lateral, or south-side-up motion on the Pinto Mountain fault. Note that the Pinto Mountain fault also localized strain due to both the Landers [*Fialko*, 2004] and the Hector Mine [*Fialko et al.*, 2002] earthquakes. The co-seismic deformation of the Pinto Mountain fault has been attributed to a 2 km wide zone of low rigidity immediately to the south of the geologically mapped surface trace of the fault. Unfortunately, the accuracy of the ascending data (Figure 16c) is insufficient to resolve the ambiguity between the horizontal and vertical displacements across the Pinto Mountain fault between 1992 and 1999. Further observations are needed to establish whether the apparent strain accumulation on the Pinto Mountain fault represents a secular deformation, or is part of the post-seismic transient.

Space geodetic data and modeling results presented in this paper reveal a complex nature of the transient deformation following the Landers earthquake. The bulk of the observed post-seismic deformation can be explained by two physical mechanisms, the percola-

tion of pore fluids through the upper crust, and the localized shear deformation on the earthquake fault and its downdip extension. Given a realistic nonlinear temperature-dependent rheology of rocks below the brittle-ductile transition, such a localized deformation is expected from visco-elasto-plastic models of post-seismic deformation, implying that there may be little phenomenological difference between the deep afterslip and viscous relaxation models. Overall, the post-Landers geodetic data are consistent with a view that the upper crustal faults are coupled to the mantle tectonics via deep trans-crustal shear zones [e.g., *Savage and Burford*, 1973; *Jackson*, 2002], and that both the lower crust and the upper mantle support long-term deviatoric stresses. The available data do not require a large-scale viscous deformation of the lower lithosphere below the ECSZ over 7 years following the Landers earthquake, implying a lower bound on the effective dynamic viscosities of the lower crust and upper mantle of the order of $10^{19} - 10^{20}$ Pa s. Continued geodetic observations over the next decade will refine this constraint on the rheologic properties of the lower lithosphere below the Mojave desert.

6. Conclusions

The space geodetic data including several tens of radar interferograms, and horizontal displacement vectors from several tens of continuous and campaign GPS sites collected in the area of the 1992 Landers earthquake between 1992 and 1999 reveal a monotonic deformation transient with a characteristic decay time of the order of several years. The horizontal post-seismic velocities appear to decay faster than the satellite line of sight velocities that are sensitive to both horizontal and vertical motion of the Earth's surface. Analysis of the spatiotemporal signatures of the observed deformation field, and comparisons with theoretical models of post-seismic relaxation suggests that the post-Landers transient is likely caused by a combination of at least two different deformation mechanisms. The deformation anomaly imaged by the InSAR is best explained in terms of the diffusion of pore fluids and the associated poro-elastic relaxation involving the bulk of the upper crust, and extending to (or below) the brittle-ductile transition (depth of 15 km). The effective hydraulic diffusivity of the upper crust inferred from the kinetics of surface deformation is of the order of 0.1-1 m^2/s, consistent with independent estimates of in situ transport properties of crystalline rocks. A second deformation mechanism is required to explain large horizontal displacements of the order of 10 cm measured with GPS in the far field ($> 30 - 40$ km away from the earthquake rupture). Modeling of space geodetic data presented in this paper shows that the fault afterslip extending from the Earth's surface to the base of the crust (or perhaps below the Moho) is a likely candidate for such a mechanism. Visco-elastic models assuming a weak upper mantle [e.g., *Pollitz et al.*, 2000, 2001] reasonably well explain a number of the GPS vectors, but overpredict fault-perpendicular displacements along the main nodal plane of the Landers rupture. Assuming a nearly complete visco-elastic relaxation, the weak mantle model predict broad areas of uplift and subsidence having amplitudes of the order of 15 cm. InSAR data demonstrate that this deformation did not occurr 7 years after the Landers earthquake, implying a lower bound on the effective mantle viscosity of the order of 10^{19} Pa s. As the surface deformation due to viscous relaxation is governed by stress changes at the base of the elastic layer, the long-term visco-elastic response to the co-seismic loading can be modeled using a computationally efficient boundary element approach. The latter can be also modified to simulate a time-dependent deformation by explicitly considering evolution of stress at the base of the elastic layer for various constitutive models of the substrate.

A lack of spatial correlation between the maximum co-seismic and post-seismic slip deduced from inversions of geodetic data suggests that the pore pressure changes associated with poro-elastic relaxation don't modulate the rate and total amount of afterslip in the upper crust. The maximum afterslip tends to occur on the periphery of high co-seismic slip patches, implying that the co-seismic stress perturbations provide the dominant controls on the dynamics of afterslip. The same conclusion holds for afterslip below the brittle-ductile transition. The deep afterslip due to the Landers earthquake tends to occur in areas of largest increases in the co-seismic shear stress below the Landers rupture. Results presented in this paper suggest that the continental lower crust, as well as the upper mantle are able to support appreciable deviatoric stress, and that major crustal faults may localize strain throughout much of the lithosphere, as envisioned in the fault-block model of crustal tectonics.

Acknowledgments.

Original SAR data are copyrighted by the European Space Agency, distributed by Eurimage, Italy, and acquired via the WInSAR Consortium with funding from NSF, NASA and USGS. The ERS SAR data were processed using the JPL/Caltech software package ROI_PAC. Observation and modeling data used in this study are available from the au-

thor. This research was supported by the Southern California Earthquake Center. SCEC is funded by NSF Cooperative Agreement EAR-0106924 and USGS Cooperative Agreement 02HQAG0008. The SCEC contribution number for this paper is 761.

References

Bock, Y., et al., Southern California Permanent GPS Geodetic Array: Continuous measurements of regional crustal deformation between the 1992 Landers and 1994 Northridge earthquakes, *J. Geophys. Res.*, *102*, 18,013–18,033, 1997.

Booker, J., Time-dependent strain following faulting of a porous-medium, *J. Geophys. Res.*, *79*, 2037–2044, 1974.

Brace, W. F., and D. L. Kohlstedt, Limits on lithospheric stress imposed by laboratory experiments, *J. Geophys. Res.*, *85*, 6248–6252, 1980.

Bürgmann, R., P. Rosen, and E. Fielding, Synthetic aperture radar interferometry to measure Earth's surface topography and its deformation, *Annu. Rev. Earth Planet. Sci.*, *28*, 169–209, 2000.

Deng, J., K. Hudnut, M. Gurnis, and E. Hauksson, Viscoelastic flow in the lower crust after the 1992 Landers, California, earthquake, *Science*, *282*, 1689–1692, 1998.

Dieterich, J. H., Earthquake nucleation on faults with rate- and state-dependent strength, *Tectonophysics*, *211*, 115–134, 1992.

Elsasser, W. M., Convection and stress propagation in the upper mantle, in *The Application of Modern Physics to the Earth and Planetary Interiors*, edited by S. K. Runcorn, pp. 223–249, Wiley, New York, 1969.

England, P. C., and P. Molnar, Active deformation of Asia: from kinematics to dynamics, *Science*, *278*, 647–650, 1997.

Fialko, Y., Probing the mechanical properties of seismically active crust with space geodesy: Study of the co-seismic deformation due to the 1992 M_w7.3 Landers (southern California) earthquake, *J. Geophys. Res.*, *109*, 10.1029/2003JB002,756, 2004.

Fialko, Y., and M. Simons, Evidence for on-going inflation of the Socorro magma body, New Mexico, from Interferometric Synthetic Aperture Radar imaging, *Geophys. Res. Lett.*, *28*, 3549–3552, 2001.

Fialko, Y., M. Simons, and D. Agnew, The complete (3-D) surface displacement field in the epicentral area of the 1999 M_w7.1 Hector Mine earthquake, southern California, from space geodetic observations, *Geophys. Res. Lett.*, *28*, 3063–3066, 2001.

Fialko, Y., D. Sandwell, D. Agnew, M. Simons, P. Shearer, and B. Minster, Deformation on nearby faults induced by the 1999 Hector Mine earthquake, *Science*, *297*, 1858–1862, 2002.

Fialko, Y. A., and A. M. Rubin, What controls the along-strike slopes of volcanic rift zones?, *J. Geophys. Res.*, *104*, 20,007–20,020, 1999.

Fleitout, L., and C. Froidevaux, Thermal and mechanical evolution of shear zones, *J. Struct. Geol.*, *2*, 159–164, 1980.

Goldstein, R. M., Atmospheric limitations to repeat-track radar interferometry, *Geophys. Res. Lett.*, *22*, 2517–2520, 1995.

Gordon, D., C. Ma, and W. Ryan, Results from the CDP Mobile VLBI Program in the western United States, in *Contributions of space geodesy to geodynamics: Crustal dynamics*, edited by D. Smith and D. Turcotte, pp. 131–138, AGU, Washington D.C., 1993.

Healy, J., W. W. Rubey, D. T. Griggs, and C. B. Raleigh, The Denver earthquakes, *Science*, *161*, 1301–1310, 1968.

Hearn, E. H., What can GPS data tell us about the dynamics of post-seismic deformation?, *Geophys. J. Int.*, *155*, 753–777, 2003.

Hoang, D., T. Becker, S. Kenner, and Y. Fialko, Finite element and boundary element benchmarks for the post-seismic deformation, *Proc. Ann. SCEC Meeting*, p. 71, 2003.

Hudnut, K. W., et al., Co-seismic displacements in the Landers sequence, *Bull. Seismol. Soc. Am.*, *84*, 625–645, 1994.

Ivins, E., Transient creep of a composite lower crust. 2. a polymineralic basis for rapidly evolving postseismic deformation models, *J. Geophys. Res.*, *101*, 28,005–28,028, 1996.

Jackson, J., Strength of the continental lithosphere: Time to abandon the jelly sandwich?, *GSA Today*, *12*, 4–9, 2002.

Jacobs, A., D. Sandwell, Y. Fialko, and L. Sichoix, The 1999 (M_w7.1) Hector Mine, California, earthquake: Near-field postseismic deformation from ERS interferometry, *Bull. Seism. Soc. Am.*, *92*, 1433–1442, 2002.

Jennings, C., *Fault activity map of California and adjacent areas, with locations and ages of recent volcanic eruptions*, California Division of Mines and Geology, Geologic Data Map No. 6, map scale 1:750,000, 1994.

Jones, L., and D. Helmberger, Earthquake source parameters and fault kinematics in the eastern California shear zone, *Bull. Seism. Soc. Am.*, *88*, 1337–1352, 1998.

Jonsson, S., P. Segall, R. Pedersen, and G. Bjornsson, Post-earthquake ground movements correlated to pore-pressure transients, *Nature*, *424*, 179–183, 2003.

Kirby, S., Rheology of the lithosphere, *Rev. Geophys.*, *21*, 1458–1487, 1983.

Kohlstedt, D. L., B. Evans, and S. J. Mackwell, Strength of the lithosphere: Constraints imposed by laboratory experiments, *J. Geophys. Res.*, *100*, 17,587–17,602, 1995.

Lamb, S., Is it all in the crust?, *Nature*, *420*, 130–131, 2002.

Mainprice, D., and M. Paterson, Experimental studies of the role of water in the plasticity of quartzites, *J. Geophys. Res.*, *89*, 4257–4270, 1984.

Massonnet, D., and K. Feigl, Radar interferometry and its application to changes in the Earth's surface, *Rev. Geophys.*, *36*, 441–500, 1998.

Massonnet, D., K. Feigl, M. Rossi, and F. Adragna, Radar interferometric mapping of deformation in the year after the Landers earthquake, *Nature*, *369*, 227–230, 1994.

Massonnet, D., W. Thatcher, and H. Vadon, Detection of postseismic fault-zone collapse following the Landers earthquake, *Nature*, *382*, 612–616, 1996.

Masterlark, T., and H. Wang, Transient stress-coupling between the 1992 Landers and 1999 Hector Mine, California, earthquakes, *Bull. Seism. Soc. Am.*, *92*, 1470–1486, 2002.

Mendoza, C., and C. Hartzell, Aftershock patterns and main shock faulting, *Bull. Seism. Soc. Am.*, *78*, 1438–1449, 1988.

Nikolaevskiy, V., K. Vasniev, A. Gorbunov, and G. Zotov, *Mechanics of saturated porous media*, 342 pp., Nedra, Moscow, in Russian, 1970.

Peltzer, G., P. Rosen, F. Rogez, and K. Hudnut, Postseismic rebound in fault step-overs caused by pore fluid flow, *Science*, *273*, 1202–1204, 1996.

Peltzer, G., P. Rosen, F. Rogez, and K. Hudnut, Poroelastic rebound along the Landers 1992 earthquake surface rupture, *J. Geophys. Res.*, *103*, 30,131–30,145, 1998.

Peltzer, G., F. Crampe, S. Hensley, and P. Rosen, Transient strain accumulation and fault interaction in the Eastern California shear zone, *Geology*, *29*, 975–978, 2001.

Perfettini, H., and J. Avouac, Postseismic relaxation driven by brittle creep: A possible mechanism to reconsile geodetic measurements and the decay rate of aftershocks, application to the Chi-Chi earthquake, Taiwan, *J. Geophys. Res.*, *109*, 2004.

Pollitz, F. F., Gravitational viscoelastic postseismic relaxation on a layered spherical Earth, *J. Geophys. Res.*, *102*, 17,921–17,941, 1997.

Pollitz, F. F., G. Peltzer, and R. Bürgmann, Mobility of continental mantle: Evidence from postseismic geodetic observations following the 1992 Landers earthquake, *J. Geophys. Res.*, *105*, 8035–8054, 2000.

Pollitz, F. F., C. Wicks, and W. Thatcher, Mantle flow beneath a continental strike-slip fault: Postseismic deformation after the 1999 Hector Mine earthquake, *Science*, *293*, 1814–1818, 2001.

Reilinger, R., et al., Coseismic and postseismic fault slip for the 17 August 1999, M=7.5, Izmit, Turkey earthquake, *Science*, *289*, 1519–1524, 2000.

Rice, J. R., The mechanics of earthquake rupture, in *Physics of the Earth's Interior*, edited by A. M. Dziewonski and E. Boschi, pp. 555–649, North-Holland, Amsterdam, 1980.

Rice, J. R., Fault stress states, pore pressure distribution, and the weakness of the San Andreas Fault, in *Fault mechanics and transport properties of rocks*, edited by B. Evans and T. Wong, pp. 475–503, Academic, San Diego, CA, USA, 1992.

Rice, J. R., and M. P. Cleary, Some basic stress-diffusion solutions for fluid-saturated elastic porous media with compressible constituents, *Rev. Geophys.*, *14*, 227–241, 1976.

Roeloffs, E., Fault stability changes induced beneath a reservoir with cyclic variations in water level, *J. Geophys. Res.*, *93*, 2107–2124, 1988.

Rosen, P., S. Hensley, I. Joughin, F. Li, S. Madsen, E. Rodriguez, and R. Goldstein, Synthetic aperture radar interferometry, *Proc. of the IEEE*, *88*, 333–382, 2000.

Rothert, E., S. Shapiro, S. Buske, and M. Bohnhoff, Mutual relationship between microseismicity and seismic reflectivity: Case study at the German Continental Deep Drilling Site (KTB), *Geophys. Res. Lett.*, *30*, 10.1029/2003GL017,848, 2003.

Rubin, A. M., Dike-induced faulting and graben subsidence in volcanic rift zones, *J. Geophys. Res.*, *97*, 1839–1858, 1992.

Ruina, A., Slip instability and state variable friction laws, *J. Geophys. Res.*, *88*, 10,359–10,370, 1983.

Savage, J., and R. Burford, Geodetic determination of relative plate motion in central California, *J. Geophys. Res.*, *78*, 832–845, 1973.

Savage, J., and J. Church, Evidence for postearthquake slip in Fairview Peak, Dixie Valley, and Rainbow Mountain fault areas of Nevada, *Bull. Seism. Soc. Am.*, *64*, 687–698, 1974.

Savage, J., and J. Svarc, Postseismic deformation associated with the 1992 M_w=7.3 Landers earthquake, southern California, *J. Geophys. Res.*, *102*, 7565–7577, 1997.

Savage, J. C., Equivalent strike-slip earthquake cycles in half-space and lithosphere-asthenosphere earth models, *J. Geophys. Res.*, *95*, 4873–4879, 1990.

Savage, J. C., and W. H. Prescott, Asthenosphere readjustment and the earthquake cycle, *J. Geophys. Res.*, *83*, 3369–3376, 1981.

Savage, J. C., J. Svarc, and W. H. Prescott, Near-field postseismic deformation associated with the 1992 landers and 1999 hector mine, california, earthquakes, *J. Geophys. Res.*, *108*, 10.1029/2002JB002,330, 2003.

Shen, Z., D. Jackson, Y. Feng, M. Cline, M. Kim, P. Fang, and Y. Bock, Postseismic deformation following the Landers earthquake, California, 28 June 1992, *Bull. Seism. Soc. Am.*, *84*, 780–791, 1994.

Shimamoto, T., A transition between frictional slip and ductile flow undergoing large shear deformation at room temperature, *Science*, *231*, 711–714, 1986.

Simons, M., Y. Fialko, and L. Rivera, Coseismic deformation from the 1999 M_w7.1 Hector Mine, California, earthquake, as inferred from InSAR and GPS observations, *Bull. Seism. Soc. Am.*, *92*, 1390–1402, 2002.

Simpson, D., W. Leith, and C. Scholz, 2 types of reservoir-induced seismicity, *Bull. Seism. Soc. Am.*, *78*, 2025–2040, 1988.

Smith, B., and D. Sandwell, Coulomb stress accumulation along the san andreas fault system, *J. Geophys. Res.*, *108*, 10.1029/2002JB002,296, 2003.

Talwani, P., J. Cobb, and M. Schaeffer, In situ measurements of hydraulic properties of a shear zone in northwestern South Carolina, *J. Geophys. Res.*, *104*, 14,993–15,003, 1999.

Tarayre, H., and D. Massonnet, Atmospheric propagation heterogeneities revealed by ERS-1 interferometry, *Geophys. Res. Lett.*, *23*, 989–992, 1996.

Thatcher, W., Nonlinear strain build-up and the earthquake cycle on the San Andreas fault, *J. Geophys. Res.*, *88*, 5893–5902, 1983.

Tse, S. T., and J. R. Rice, Crustal earthquake instability in relation to the depth variation of frictional slip properties, *J. Geophys. Res.*, *91*, 9452–9472, 1986.

Tullis, J., and R. Yund, Transition from cataclastic flow to dislocation creep of feldspar, *Geology*, *15*, 606–09, 1987.

Turcotte, D. L., and G. Schubert, *Geodynamics, 2nd ed.*, 456 pp., Cambridge Univ., New York, NY, 2002.

Wald, D. J., and T. H. Heaton, Spatial and temporal distribution of slip for the 1992 Landers, California, earthquake, *Bull. Seismol. Soc. Am.*, *84*, 668–691, 1994.

Wang, H., *Theory of linear poroelasticity: With applications to geomechanics*, 287 pp., Princeton Univ. Press, Princeton, New Jersey, 2000.

Wang, R., F. Martin, and F. Roth, Computation of deformation induced by earthquakes in a multi-layered elastic crust - FORTRAN programs EDGRN/EDCMP, *Comp. Geosci.*, *29*, 195–207, 2003.

Yagi, Y., M. Kikuchi, and T. Sagiya, Co-seismic slip, post-seismic slip, and aftershocks associated with two earthquakes in 1996 in Hyuga-nada, Japan, *Earth Planets Space*, *53*, 793–803, 2001.

Yuen, D., L. Fleitout, G. Schubert, and C. Froidevaux, Shear deformation zones along major transform faults and subducting slabs, *Geophys. J. R. Astron. Soc.*, *54*, 93–119, 1978.

Zebker, H. A., P. A. Rosen, and S. Hensley, Atmospheric effects in interferometric synthetic aperture radar surface deformation and topographic maps, *J. Geophys. Res.*, *102*, 7547–7563, 1997.

Y. Fialko, Institute of Geophysics and Planetary Physics, Scripps Institution of Oceanography, University of California San Diego, La Jolla, CA 92093. (e-mail: fialko@radar.ucsd.edu)

Received 20 January 2004; revised 29 April 2004; accepted 18 May 2004.